Supporting Information

Electronic Structure Modification of SnO_2 to Accelerate CO_2 Reduction towards Formate

Lulu Li[a,b], Shican Wu[a,b], Dongfang Cheng[c], Zhi-Jian Zhao*[a,b,d], and Jinlong Gong*[a,b,d,e,f]

[a]*Key Laboratory for Green Chemical Technology of Ministry of Education, School of Chemical Engineering & Technology, Tianjin University, Tianjin 300072, China.*

[b]*Collaborative Innovation Center for Chemical Science & Engineering (Tianjin), Tianjin 300072, China.*

[c]*Department of Chemical and Biomolecular Engineering, University of California, Los Angeles, California 90095, United states.*

[d]*Joint School of National University of Singapore and Tianjin University, International Campus of Tianjin University, Binhai New City, Fuzhou 350207, China.*

[e]*Haihe Laboratory of Sustainable Chemical Transformations, Tianjin 300192, China*

[f]*National Industry-Education Platform of Energy Storage, Tianjin University, 135 Yaguan Road, Tianjin300350, China*

*E-mail: jilong@tju.edu.cn, zjzhao@tju.edu.cn

Computational Methods

All computational simulations were executed utilizing the Vienna Ab-Initio Simulation Package (VASP) [1]. The description of the interaction between valence electrons and the ionic core employed the Projector-Augmented Wave (PAW) method [2]. within the framework of the Perdew, Burke, and Ernzerhof (PBE) exchange–correlation functional [3]. To account for the absence of van der Waals interactions in the GGA functional, the Grimme D3 correction was implemented [4]. The SnO_2(110) surface is selected in this work as its formation from the cleaving of the rutile phase of SnO_2 crystal with the thermodynamically lowest-energy [5]. The computational model comprised a 4-layer (4 × 2) slab, with the substitution of a Sn atom by various metal atoms (M@SnO_2) and bottom two layer fixed. Building upon prior studies, it has been established that the bridge oxygen on the SnO_2(110) surface is stable only in the form of hydroxyl (OH) under the aqueous environment [6]. Therefore, this hydroxylated SnO_2(110) surface is performed and exhibits a single possible active Sn site. It is important to note that due to the large variation in the atomic radius of the dopant M from the element periodical table, doping SnO_2(110) surfaces can lead to some degree of surface relaxation in the vertical direction. However, the overall surface does not undergo any substantial reconstruction.

In this work, convergence criteria for electronic and force minimization were set at 10^{-6} eV and 0.02 eV/Å, respectively, during the structural optimization. The cutoff energy for the kinetic energy of the plane-waves was set to 650 eV. Moreover, a vacuum layer of at least 15 Å was included for SnO_2(110) slab. The Brillouin zone was sampled using a 3 × 3 × 1 Monkhorst-Pack k-point grid for slab and 15 × 15 × 15 Monkhorst-Pack k-point grid for bulk.

The doping includes 48 metals, namely, Li, Be, Na, Mg, Al, K, Ca, Sc, Ti, V, Cr, Mn, Fe, Co, Ni, Zn, Ga, Ge, Rb, Sr, Y, Zr, Nb, Mo, Ru, Rh, Pd, Ag, Cd, In, Sb, Cs, Ba, La, Nd, Gd, Hf, Ta, W,

Re, Os, Ir, Pt, Au, Hg, Tl, Pb, and Bi. The formation energy is calculated from the following formula:

$$E(M@SnO_2) + E(Sn_{atom}) - E(SnO_2) - E(M_{atom}) \quad \text{(S-1)}$$

where the energies of Sn_{atom} and M_{atom} are both derived from the energies of the bulk structures of Sn and the metal, $E_{atom} = E_{bulk} / N$, where N is the number of atoms in the bulk structure. It's worth noting that in this work, only the La element was selected as a representative of the lanthanide series. Moreover, literature has found that doping with La not only introduces geometric lattice defects but more importantly, the addition of La engages in significant electronic interactions with the host, affecting its band and other electronic structures, thereby influencing the catalytic performance [7].

In this study, the grand canonical DFT (GCDFT) calculation was used to gain the potential-dependent energetics. In the grand canonical DFT calculation part, the Fermi level is modified by altering the electrons within the simulated system, as obtained through self-consistent electronic energy calculation. This approach allows the derivation of grand canonical energies at different Fermi levels [8,9]. Besides, the potential-dependent grand canonical energy exhibits a quadratic relationship with the potential energy: $\Omega(U) = \Omega(U_0) - 1/2C(U - U_0)^2$, where C is the surface capacitance. We utilized a linearized Poisson-Boltzmann model implemented in VASPsol to represent the polarizable electrolyte medium and keep the whole system neutral when charging the electrode.[10]. The water dielectric constant was set to 78.4 and a Debye screening length of 1 M electrolyte concentration was set to 3.0 Å. For GCDFT calculation, we focused on $Ti@SnO_2$ and $Zr@SnO_2$ as representatives, alongside pure SnO_2, to assess the grand canonical Gibbs free energy (ΔG_{GC}) of intermediates and the theoretical overpotentials required at various negative potentials.

We compute the free energy of each intermediate using the expression $G = E_{DFT} + ZPE + \delta H_0 - TS$. Here, E_{DFT} stands for the DFT total energy, ZPE accounts for the zero-point vibrational energy, δH_0 represents the integrated heat capacity, while T denotes the reaction temperature, and S signifies entropy. The entropy calculations were performed using the Harmonic oscillator approximation, detailed in Table S2. An essential aspect involves determining the theoretical overpotential, which is numerically equivalent to the absolute value of the most significant Gibbs free energy change observed during the Electrocatalytic CO_2 reduction (CO_2ER) to formate or CO and hydrogen evolution reactions (HER).

The detailed reaction mechanism of CO_2ER to formate or CO and HER include, while the * indicates adsorb site, which in this work is Sn next to the doping element:

Formate: $CO_2 + * + e^- + H^+ \rightarrow HCOO*$ (S-2)

$HCOO* + e^- + H^+ \rightarrow HCOOH$ (S-3)

CO: $CO_2 + * + e^- + H^+ \rightarrow *COOH$ (S-4)

$*COOH + e^- + H^+ \rightarrow CO + H_2O$ (S-5)

H_2: $* + e^- + H^+ \rightarrow H*$ (S-6)

It's noteworthy that CO adsorption calculations were also conducted (Table S3, Figure S2), revealing weak CO adsorption on M@SnO_2 surfaces and primarily in a physisorption form. Therefore, CO adsorption was not considered in the following reaction performance. To intuitively demonstrate the impact of doping on the electronic structure of Sn active sites, we defined the net charge of Sn as net charge = valence electrons – Bader charge [11]. A decreasing net charge indicates a more pronounced reduced state of SnO_2.

The Bader charges are calculated using Bader Charge Analysis program[12]. The crystal orbital Hamilton population (COHP) analysis was performed using the Lobster 3.2.0 code, which involves transforming the (plane) wave functions from VASP into a localized basis set [13,14].

Our study extended to ab initio molecular dynamics (AIMD) simulations, conducted at a controlled temperature of 300 K, within the canonical (NVT) ensemble [15,16]. This temperature was chosen to reflect standard operational conditions for CO_2 reduction processes. These simulations were performed over a duration of 10 picoseconds (ps) to ensure comprehensive sampling and thus robustness in our simulation data.

Lastly, the analysis utilizes an XGBoost regression model to predict transferred charges from element chemical properties [17], such as Electronegativity, Atomic Radius, Ionization Energy, and Electron Affinity. The dataset is split into training (85%) and testing (15%) sets, with a random seed for reproducibility. The model, defined with a predetermined random state for consistency, is trained on the training set and then used to predict charges on the testing set. The performance is visually evaluated by comparing predicted charges against actual values, alongside a feature importance plot to highlight influential predictors.

Table S1. Bulk energy of doping metal.

M bulk	Energy / eV	Number of bulk
Ag	-10.88	4
Al	-3.74	1
Au	-12.88	4
Ba	-3.82	2
Be	-7.53	2
Bi	-7.75	2
Ca	-7.72	4
Cd	-1.50	2
Co	-13.64	2
Cr	-18.16	2
Cs	-3.41	4
Cu	-14.88	4
Fe	-15.52	2
Ga	-11.65	4
Ge	-8.98	2
Hf	-19.92	2
Hg	-0.49	3
In	-5.10	2
Ir	-35.40	4
K	-4.19	4
La	-9.71	2
Li	-7.60	4
Mg	-3.01	2
Mn	-35.59	4
Mo	-42.07	4
Na	-5.23	4
Nb	-39.58	4
Ni	-21.64	4
Os	-22.50	2
Pb	-3.57	1
Pd	-20.86	4
Pt	-24.38	4
Rb	-3.75	4
Re	-24.85	2
Rh	-29.11	4
Ru	-18.50	2
Sb	-8.27	2
Sc	-12.40	2
Sr	-6.55	4
Ta	-23.72	2
Tc	-20.75	2
Ti	-15.52	2
Tl	-4.49	2
V	-17.88	2
W	-26.04	2
Y	-12.87	2
Zn	-2.22	2

Zr	-17.04	2

Table S2. The zero-point energy correction, enthalpy correction, and entropy correction for adsorbates and free molecules. All values are given in eV.

Adsorbates	**ZPE**	**δH_0**	**TS**
HCOO*	0.63	0.09	0.17
*COOH	0.62	0.10	0.19
H*	0.18	0.01	0.01
*CO	0.15	0.11	0.34
CO_2	0.31	0.11	0.66
CO	0.14	0.10	0.62
HCOOH	0.90	0.11	1.02
H_2O	0.58	0.10	0.66
H_2	0.28	0.09	0.40

Table S3. Adsorption free energy of CO on M@SnO_2 surfaces.

M@SnO_2	**ΔG_{*CO}**
Al	0.12
Ba	0.18
Ca	0.20
Cd	0.19
Co	0.14
Cr	0.15
Cs	0.22
Cu	0.19
Fe	0.13
Ga	0.15
Ge	0.23
Hf	0.15
In	0.20
La	-0.44
Li	0.18
Mg	0.14
Mn	0.18
Mo	0.41
Na	0.19
Nb	-0.35
Rb	0.05
Sc	0.12
Sn	0.24
Sr	0.33
Ta	-0.19
Ti	0.80
Tl	0.32
V	0.39
W	0.12
Y	0.20
Zn	0.27
Zr	0.34

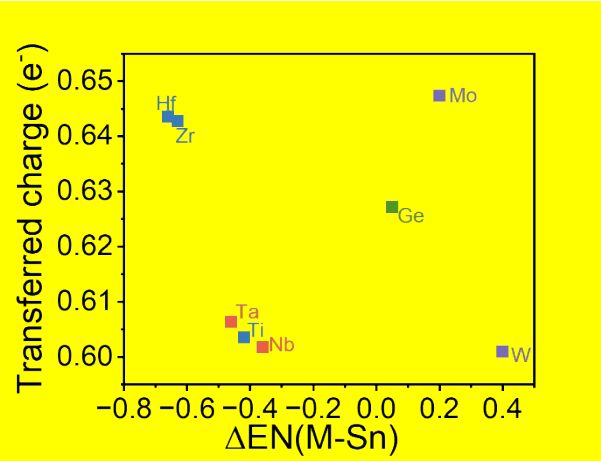

Figure S1. Correlation between transferred charge and electronegativity difference (ΔEN) between M and Sn, with elements from the same group distinguished by similar colors.

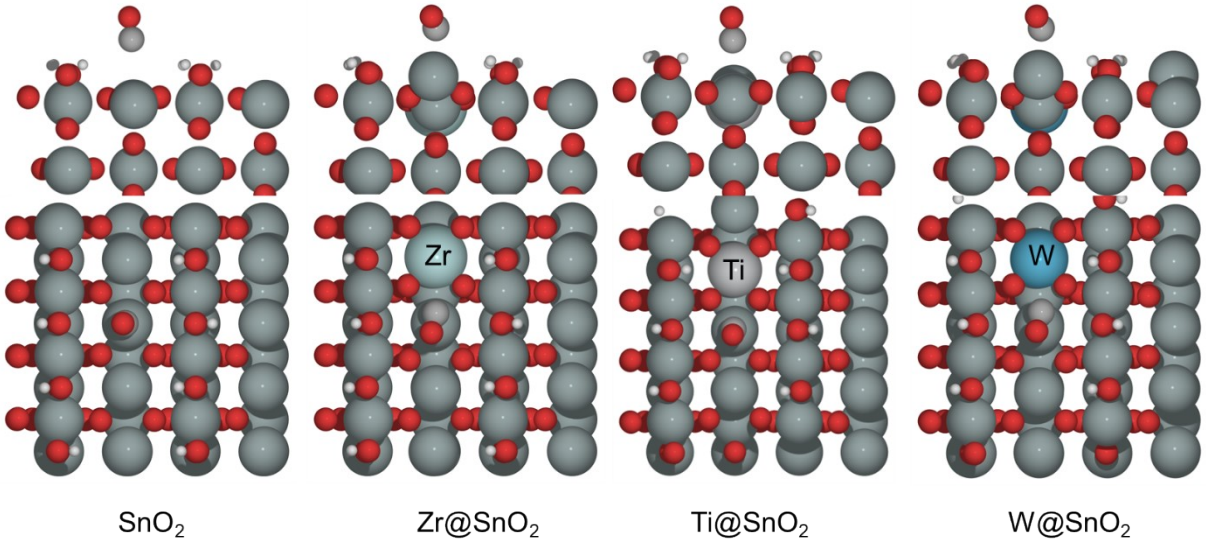

Figure S2. Adsorption configuration of CO on different M@SnO_2 structures (pure SnO_2, Zr@SnO_2, Ti@SnO_2, W@SnO_2). It can be clearly found that CO is in the form of physical adsorption on the surfaces.

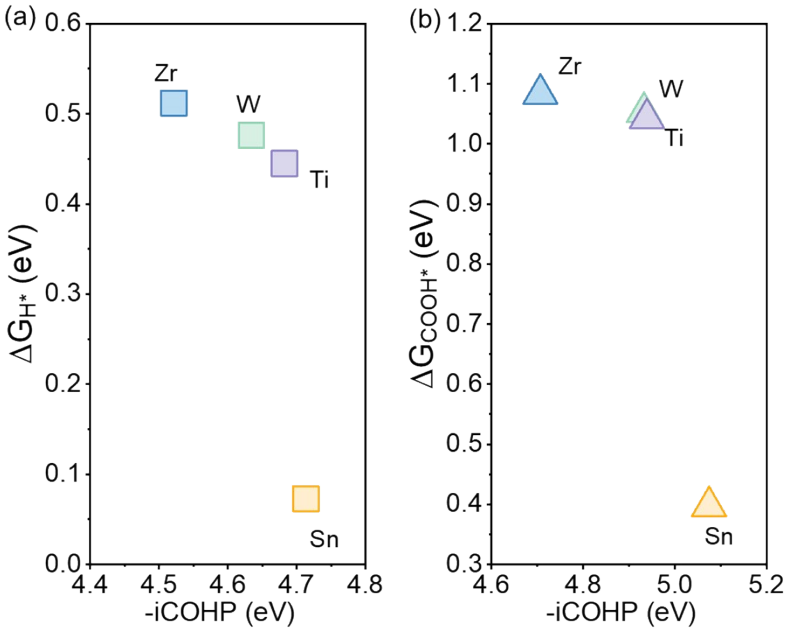

Figure S3. integrated crystal orbital Hamilton population (iCOHP) for the Sn and key intermediates on different M@SnO_2 structures, (a) H* and (b) *COOH.

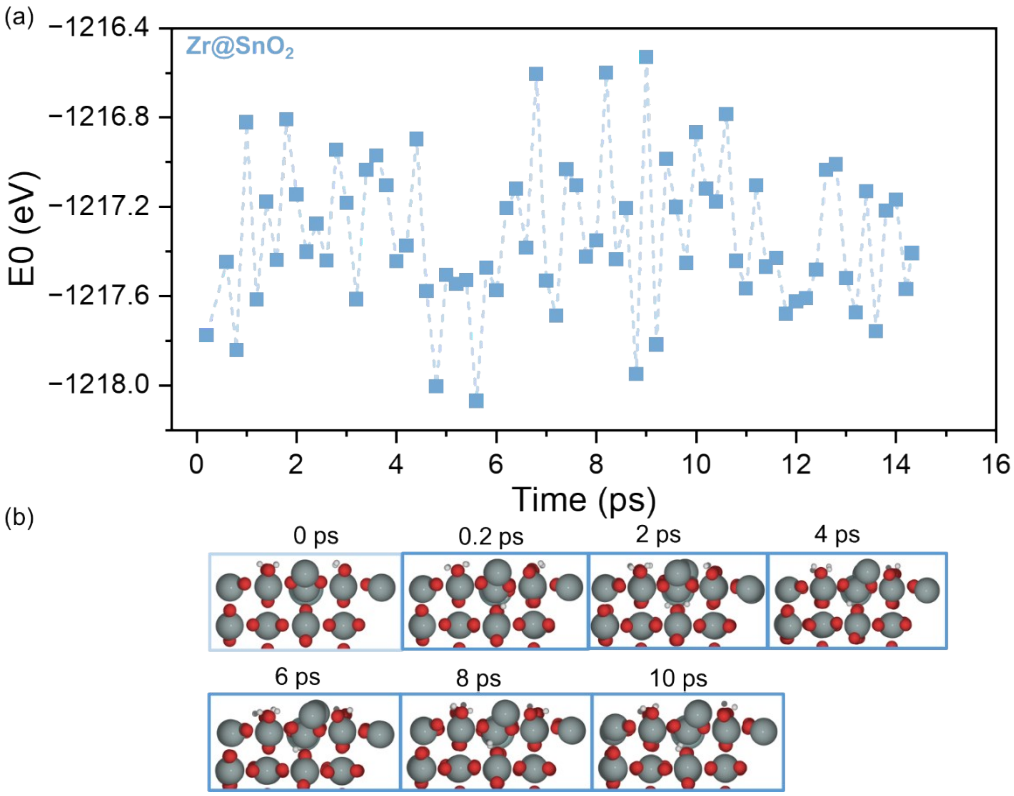

Figure S4. (a) The energy profile of $Zr@SnO_2$ AIMD simulation at 300 K. (b) The side view of the $Zr@SnO_2$ structure at different time. It is observed that starting from 0.2 ps, the hydrogen from the OH on the surface transfers to the second-layer oxygen, forming a bulk OH, which indicates the structural instability of $Zr@SnO_2$

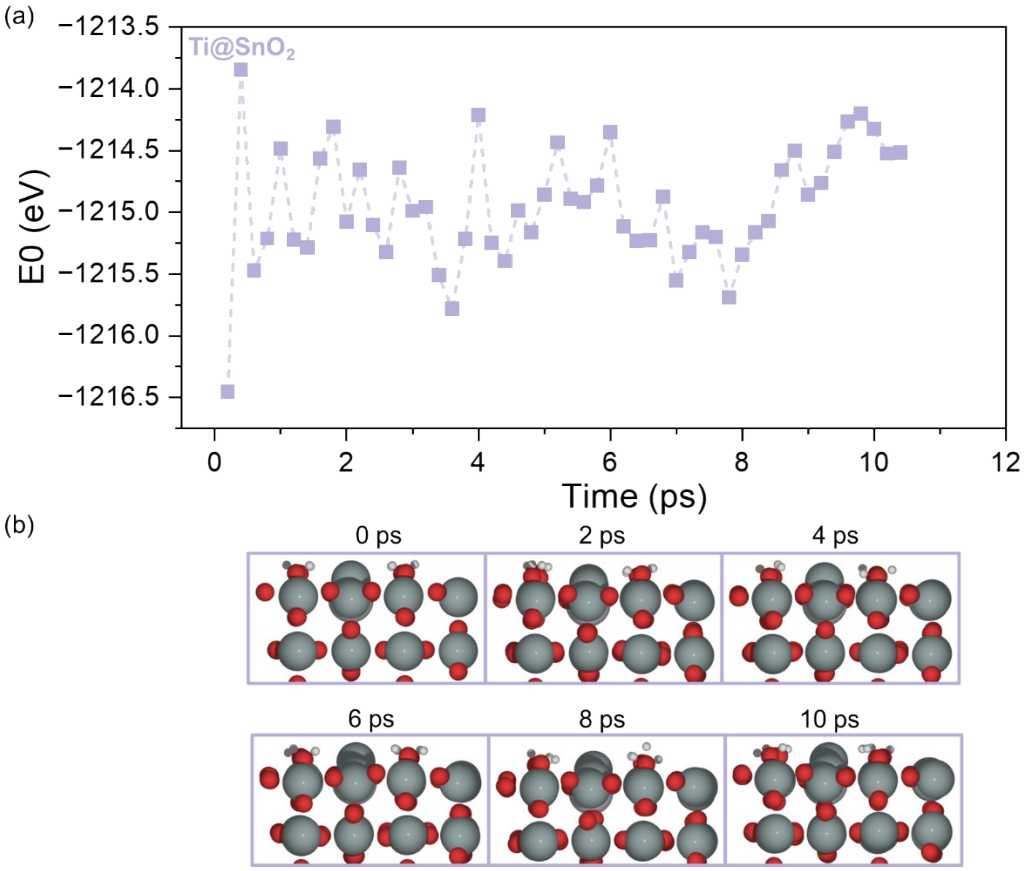

Figure S5. (a) The energy profile of $Ti@SnO_2$ AIMD simulation at 300 K. (b) The side view of the $Ti@SnO_2$ structure at 0 ps, 2 ps, 4 ps, 6 ps, 8 ps, 10 ps.

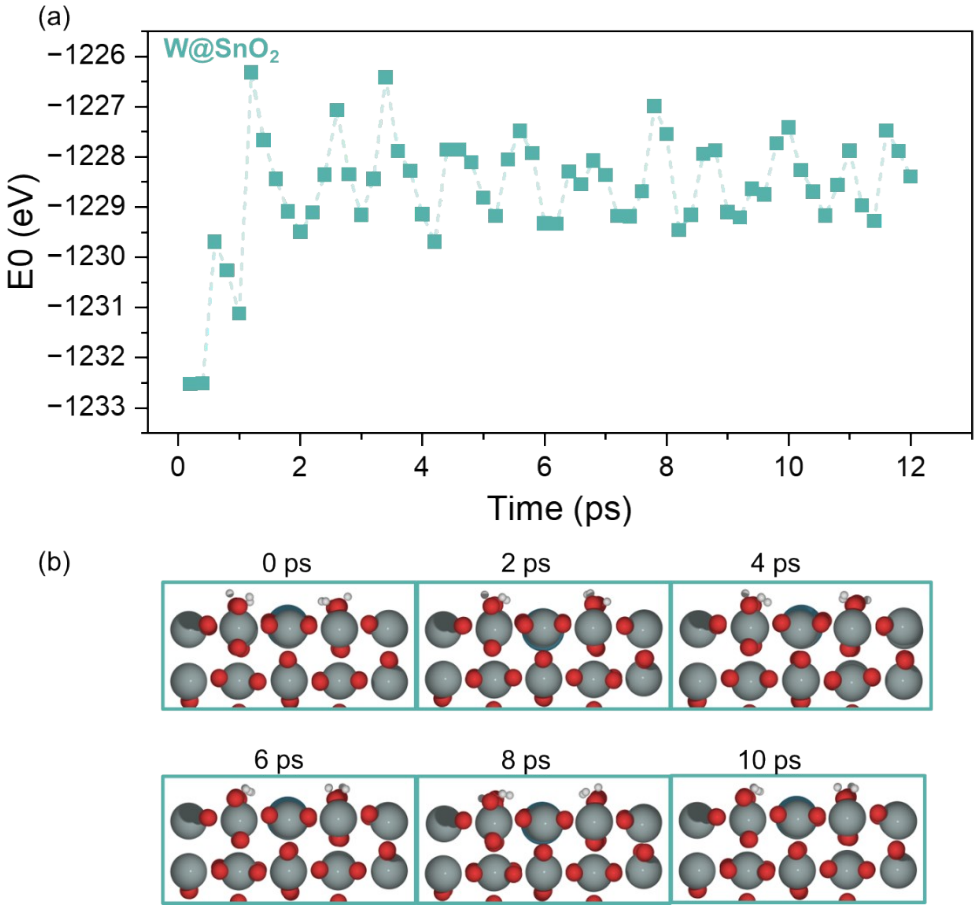

Figure S6. (a) The energy profile of $W@SnO_2$ AIMD simulation at 300 K. (b) The side view of the $W@SnO_2$ structure at 0 ps, 2 ps, 4 ps, 6 ps, 8 ps, 10 ps.

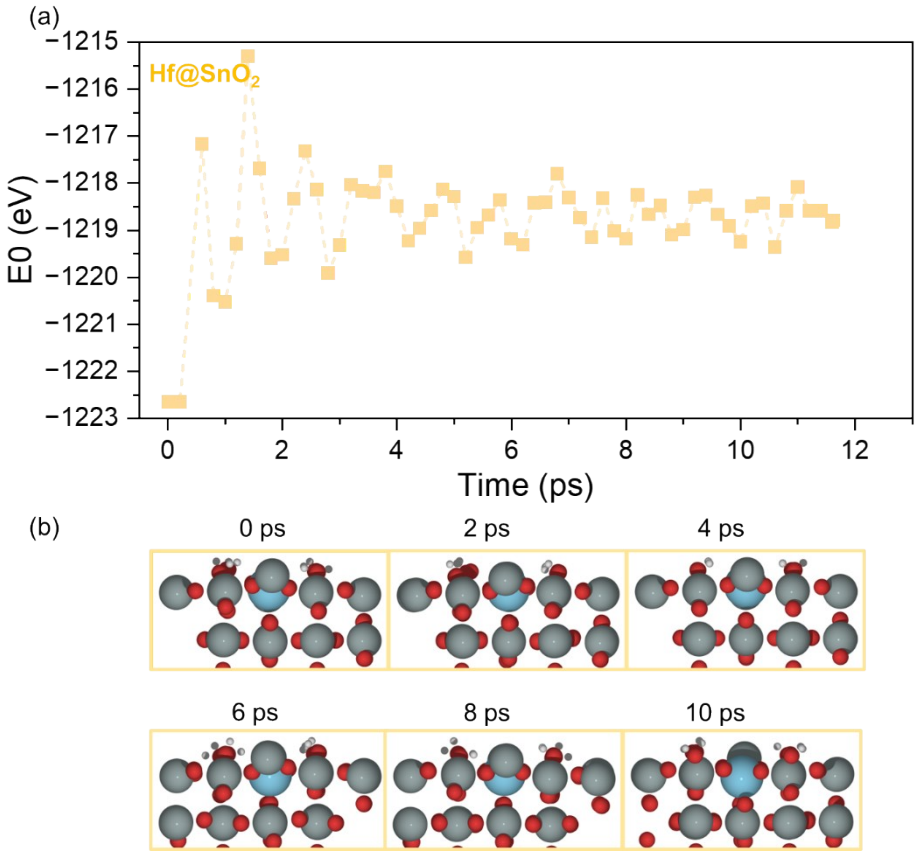

Figure S7. (a) The energy profile of $Hf@SnO_2$ AIMD simulation at 300 K. (b) The side view of the $Hf@SnO_2$ structure at 0 ps, 2 ps, 4 ps, 6 ps, 8 ps, 10 ps.

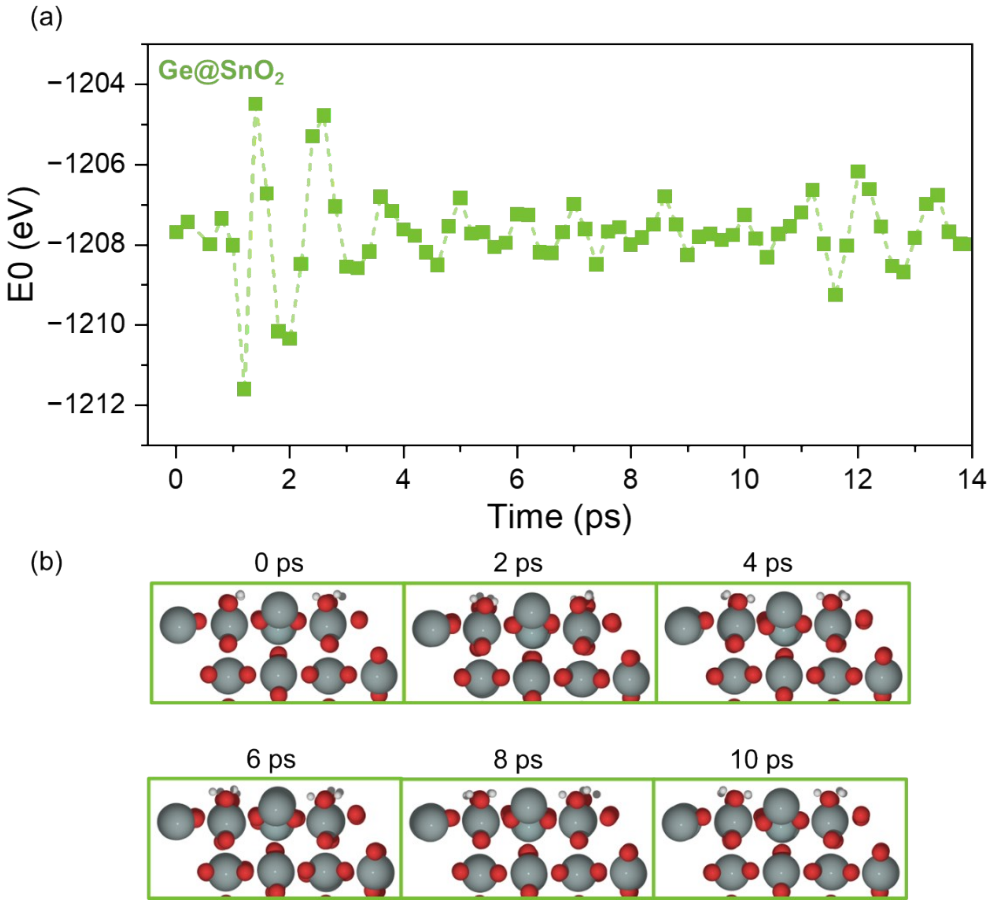

Figure S8. (a) The energy profile of $Ge@SnO_2$ AIMD simulation at 300 K. (b) The side view of the $Ge@SnO_2$ structure at 0 ps, 2 ps, 4 ps, 6 ps, 8 ps, 10 ps.

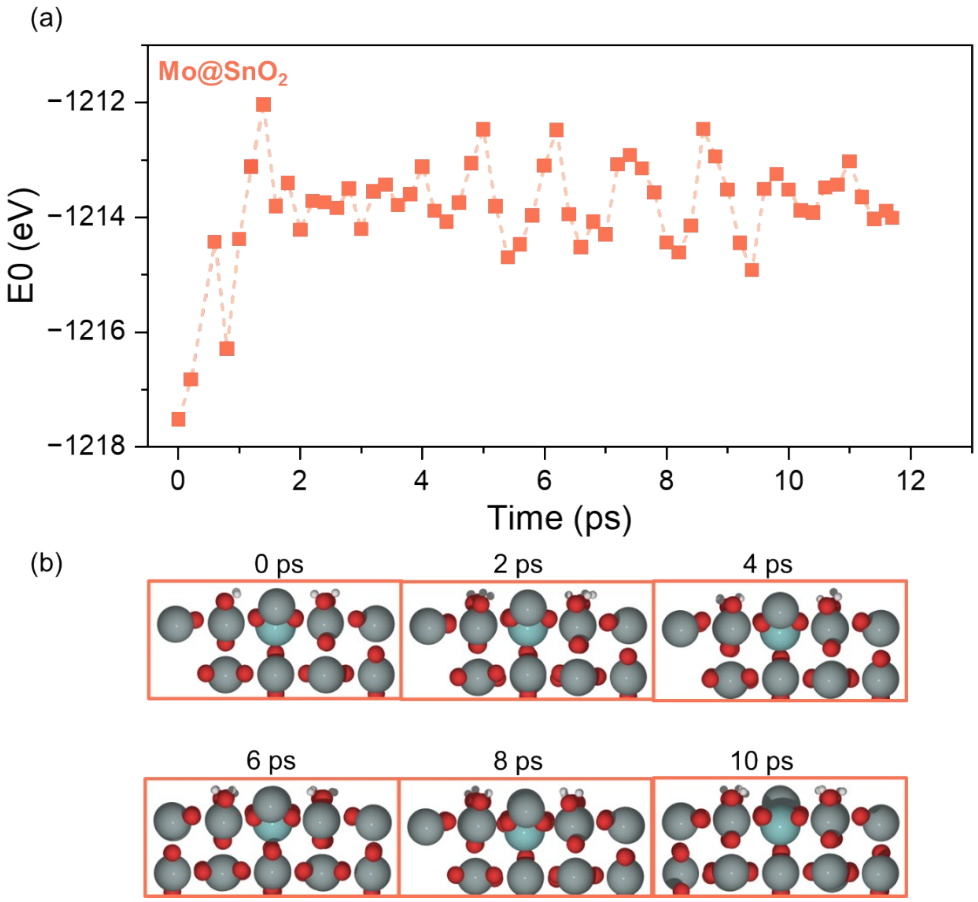

Figure S9. (a) The energy profile of $Mo@SnO_2$ AIMD simulation at 300 K. (b) The side view of the $Mo@SnO_2$ structure at 0 ps, 2 ps, 4 ps, 6 ps, 8 ps, 10 ps.

References

1 G. Kresse and J. Furthmüller, *Comput. Mater. Sci.*, 1996, **6**, 15–50.
2 P. E. Blöchl, *Phys. Rev. B*, 1994, **50**, 17953–17979.
3 G. Kresse and D. Joubert, *Phys. Rev. B*, 1999, **59**, 1758–1775.
4 S. Grimme, S. Ehrlich and L. Goerigk, *J. Comput. Chem.*, 2011, **32**, 1456–1465.
5 M. Batzill, K. Katsiev and U. Diebold, *Surf. Sci.*, 2003, **529**, 295–311.
6 Z. Liu, X. Zong, D. G. Vlachos, I. A. W. Filot and E. J. M. Hensen, *Chin. J. Catal.*, 2023, **50**, 249–259.
7 J. Xu, F. Huo, Y. Zhao, Y. Liu, Q. Yang, Y. Cheng, S. Min, Z. Jin and Z. Xiang, *Int. J. Hydrog. Energy*, 2018, **43**, 8674–8682.
8 S. N. Steinmann and P. Sautet, *J. Phys. Chem. C*, 2016, **120**, 5619–5623.
9 S. N. Steinmann, C. Michel, R. Schwiedernoch and P. Sautet, *Phys. Chem. Chem. Phys.*, 2015, **17**, 13949–13963.
10 K. Mathew, V. S. C. Kolluru, S. Mula, S. N. Steinmann and R. G. Hennig, *J. Chem. Phys.*, 2019, **151**, 234101.
11 L. Li, Z.-J. Zhao, G. Zhang, D. Cheng, X. Chang, X. Yuan, T. Wang and J. Gong, *Research*, 2023, **6**, 0067.
12 M. Yu and D. R. Trinkle, *J. Chem. Phys.*, 2011, **134**, 064111.
13 V. L. Deringer, A. L. Tchougréeff and R. Dronskowski, *J. Phys. Chem. A*, 2011, **115**, 5461–5466.
14 S. Steinberg and R. Dronskowski, *Crystals*, 2018, **8**, 225.
15 W. G. Hoover, *Phys. Rev. A*, 1985, **31**, 1695–1697.
16 R. Car and M. Parrinello, *Phys. Rev. Lett.*, 1985, **55**, 2471–2474.
17 T. Chen and C. Guestrin, in *Proceedings of the 22nd ACM SIGKDD International Conference on Knowledge Discovery and Data Mining*, Association for Computing Machinery, New York, NY, USA, 2016, pp. 785–794.